The Influence Of Rotor Separation On The Performance Of A Dual-Rotor Wind Turbine

Anthony A. Adeyanju

Department of Mechanical and Manufacturing Engineering,
University of West Indies, St. Augustine, Trinidad
Email: anthony.adeyanju@sta.uwi.edu

Abstract

The influence of rotor separation on the operation of a dual rotor horizontal axis wind turbine was explored utilizing simulation and experimental investigations. A NACA 64-315 air foil was found to be the preferred option after an air analysis was carried out to optimize the blades for Trinidad's particular environment. The simulation was conducted using the QBlade program, and the power flow performance for various wind speed iterations was found for the design. With rotor separations ranging from 0.25 meter to 3 meter at 0.25 meters' intervals, the effect of rotor separation on the performance of a dual rotor wind turbine was investigated at a fan speed of 1 m/s. The maximum tip speed ratio occurs at the smallest rotor separation distance (0.25 m), whilst the smallest tip speed ratio occurs at the largest rotor separation distance (3 m). The power coefficient (CP) and total power both increase as rotor spacing lowers, contributing to the high energy output of the dual rotor horizontal axis wind turbine.

Keywords: Dual rotor, Rotor separation, Power Coefficient, QBlade software

Introduction

Environmental concerns have increased in recent decades as the world's fossil fuel supplies have been increasingly exhausted. As a result, environmental sustainability and renewable sources are now prioritized for the stability of the global energy supply. To accomplish long-term power generation, renewable energy sources like hydro, solar, wind, bioenergy, geothermal, and others were developed and improved. The International Renewable Energy Agency (IRENA) reports that as of the end of 2019, the total capacity of renewable energy worldwide was 2537 GW, accounting for 34.7% of the world's total energy capacity [1], an increase of 7.4% (176 GW) from wind energy's contribution of 2.5% in 2018 [1]. The Global Wind Energy Council (GWEC) thus predicted a ten percent increase in worldwide wind energy generation at the end of 2019 and a mean annual increase of 9.2% over the next five years [2]. Such a

projection in wind energy development has been shown to be driven by the need for bigger turbines. Modern multi-megawatt wind turbines may generate up to 15 MW of electricity and are more than 200 meters in diameter [3].

With just one rotor, wind turbines really capture the kinetic energy of the wind. Although dual rotor wind turbines are common, they only provide one power output due to the usage of counter-rotating propellers. Additionally, the propellers have only one dimension, which prevents the most efficient utilization of all available wind energy. On a wind turbine, the airstream after the first rotor travels slower than the airstream before the first rotor, indicating that the airstream after the rotor is greater because the rotor generates power from the wind kinetic energy (KE). To collect both this wind and the additional wind passing through the first rotor, the second rotor should be bigger.

Additionally, there is a need for creating varied voltages or combinations of alternating current (AC) and direct current (DC) electrical power, as well as running various combinations of generators, pumps, and compressors, from a single wind turbine.

Therefore, a dual rotor wind turbine that efficiently captures the wind KE which can tolerate a range of wind speeds is preferred.

Numerous research papers on the utilization of dual rotor wind energy have been published, although the majority of the researchers employed the counter rotating rotor in their studies.

A main rotor's location (from 0.3 to 0.65 degrees) and the use of a counter rotor with a different diameter were shown to boost power production by up to 9.67% by Kumar et al. [4]. The power curve and the impact of the diameter and distance between the dual rotors were computed by Jung et al. [5] for a 30 kilowatt counter rotor system.

Oprina et al. [6] evaluated the rotor effectiveness of a counter-rotating wind turbine. Theoretical simulations show that compared to a single rotor, the power coefficient of multi-rotors of the same circumference may be enhanced by around 13%. The paper's drawbacks were disclosed via flow visualization, which from a distance of half a disc diameter revealed false results.

To maximize the amount of power extracted from the wind, a theoretical model is put forth that takes into account two rotors that are smaller in size than the front rotor and are positioned near the interior blade region of the mains rotor [7, 8]. The upstream rotor's center, which makes up 76.2 percent of its diameter and lacks any blades, does not capture wind energy. Further calculations reveal that the induction velocities affect the theoretical power coefficient. The total C_P was 0.814 for the analysis. When comparative analysis with a single rotor layout is carried out, the device is more efficient between 16 rpm to 60 rpm, increases wind energy extraction by up to 40 percent, and decreases bending stress over the

tower [9]. In order to attain a net power coefficient of 7%, the secondary rotor is supposed to be twenty-five percent the size of the primary rotor and axially separated by 0.2 times radius of the primary rotor, based on calculations [10].

According to Milind Deotale [11], the effectiveness of the entire system reaches a maximum of 60 % at elevated wind speeds but subsequently decreases to 28% from 30% at lower wind speeds. The average performance is just 45 percent at high speeds, though.

This study examined the performance of a dual rotor horizontal axis wind turbine (DRHAWT) using simulation and experimental analysis to ascertain the impact of rotor separation.

Performance Models Estimation

Two performance models were utilized to estimate the performance model: the 2-d Blade Element Momentum Theory, which was calculated, and the 3-d Prandtl Post-Stall, which takes rotational losses into consideration. Given that the Post-Stall model necessitates a substantial amount of data input and iterations, it was created for simulation in Q blade. These techniques are normally employed for turbines that are single-rotor to study the rotational effect; nevertheless, the Jensen Wake Model can be utilized to alter the entrance velocity for the secondary rotor using the induced wake velocity [12]. The chord (c) assumption was developed in order to find the appropriate tip speed ratio; the tip speed ratio may then be modified by varying the blade chord length. Table 1 presents the technical characteristics for the dual-rotor wind turbine.

Table 1: The dual rotor wind turbine's specifications [12]

Rotor Parameters	Primary Rotor	Secondary Rotor
Number of Blades (N_b)	3	3
Blade Length (m)	0.5	0.5
Rotor Position	Upwind	Downwind
Airfoil	NACA 64-315	NACA 64-315
Angle of Attack (α)	6	-6
Rotation	Clockwise	Counter-Clockwise
Twist (β) - degree	5	5

2.1. Theory of Blade Element Momentum (BEM)

This model applies the fundamental science of the momentum theory; it postulates that the blade may be divided into an infinitesimally small number of sections (dr). As a result, the change in axial force may be characterized as follows using the idea of angular momentum conservation:

$$dN = \frac{\rho}{2} * \frac{V_0{}^2(1-a)^2}{sin^2\emptyset} N_b(C_L cos\emptyset + C_D sin\emptyset)cdr \text{ ....} \quad (1)$$

Where, V_0 is the wind velocity upstream and c is the airfoil chord, ϕ (α+β) is the flow angle. The following equation may be used to define the torque that a *dr* element produces:

$$dT = \frac{\rho}{2} * \frac{V_0(1-a)}{sin\emptyset}\frac{\omega r(1+a')}{cos\emptyset} N_b(C_L cos\emptyset - C_D sin\emptyset)crdr \text{ ..} \quad (2)$$

Where, *r* is the local rotor radius and ω is the angular velocity of the element.

According to airfoil selection, the lift coefficient (C_L) and drag coefficient (C_D) of the NACA 64315 are 0.7735 and 0.006344, respectively, at an angle of attack of 6°.

The axial (a) and tangential factors (a'), which are depicted in the following equation, are another significant variable that was calculated in the performance model:

$$a = \frac{1}{\frac{4Fsin^2\emptyset}{\frac{cN_b}{2\pi r}(C_L cos\emptyset + C_D sin\emptyset)}+1} \text{ ....} \quad (3)$$

$$a' = \frac{1}{2}\left[\left(\sqrt{1 + \frac{4}{\lambda_r{}^2}a(1-a)}\right) - 1\right] \text{ ....} \quad (4)$$

where λr denotes the ratio of local tip speeds and in equation (5), F is the Prandtl's Tip Loss Factor, which is determined by:

$$F = \frac{2}{\pi}cos^{-1}(e^{-\frac{N_b(R-r)}{2rsin\phi}}) \text{ ....} \quad (5)$$

Using equations (3), (4), and (5), the values for (a'), (a) and (F) for various tip speed ratio were calculated. Equation (6) is used to get the total rotor power coefficient (C_P) once 'a' has been computed from each section [13]:

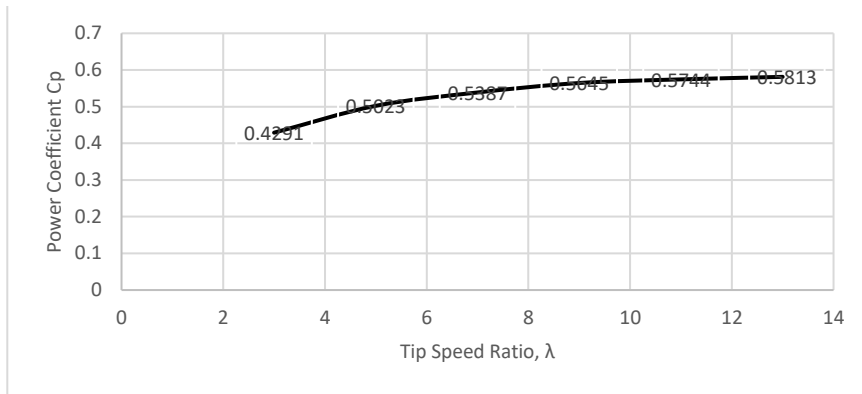$$C_p = \left(\frac{8}{\lambda^2}\right) \int_{\lambda_r}^{\lambda} \lambda_r a'(1-a)\left[1 - \left(\frac{C_d}{C_l}\right)cot\phi\right] d\lambda_r \text{ ....} \quad (6)$$

The predicted power coefficients are displayed in Table 2 through tweaking the tip speed ratio.

Table 2: Predicted Primary Rotor Power Coefficients

Tip Speed Ratio, λ	3	5	7	9	11	13
Power Coefficient C_P	0.4291	0.5021	0.5367	0.5641	0.5744	0.5813
$\frac{dC_p}{d\lambda}$	-	0.0366	0.0182	0.0129	0.0050	0.00343

Fig. 1. Predicted Primary Rotor Power Coefficients

The power coefficient increases together with the tip speed ratio, as shown in Fig. 1. Therefore, Cp converges to Betz Limit (0.593) as λ tends to infinity. However, because a tip speed ratio of 9 achieves a compromise between the highest Cp and the greatest differential value, it avoids the large cyclic loads and unstable rotating forces that high tip speed ratios produce, which might lead to mechanical malfunctions in high-speed winds.

using λ, thrust coefficient (Ct) and the axial induction factor (a), was obtained:

a = 0.1904, Ct = 0.6086

Using (a), the velocities at entry and exit of the rotor was obtained:

$v_2 = v_1(1-2a)$, then $v_2 = 0.6192v_1$

The rotor 2 inlet velocity would differ if the free velocity were similar as the wake-induced velocity because of eddy currents and vortices produced by turbulent conditions from the areas of high pressure of the rotor's tips. The Jensen Wake theory was utilized to compute the discrepancy between the actuator disk prognosis and the wake-induced number as a consequence [12]:

$$\delta v_w = v_2\left(1 - \sqrt{1 - C_t}\right)\left(\frac{D}{D+2k_wx}\right)\frac{A_{overlap}}{A} \ldots\ldots\ldots\ldots \quad (7)$$

Where, k_w is the wake decay constant, x is the axial distance that separates the disks, D is the rotor diameter, $A_{overlap}$ is the portion of the secondary disk that the area (A) of the first disk covers. The ratio between the areas is 1 due to the coaxial design of the two rotors.

The wake decay constant is:

$$k_w = \frac{0.5}{\ln\left(\frac{h}{z_0}\right)} \ldots\ldots\ldots\ldots\ldots\ldots\ldots\ldots\ldots\ldots\ldots\ldots\ldots\ldots\ldots\ldots \quad (8)$$

$$z_0 = e^{\frac{u_2 ln(h_2) - u_1 \ln(h_1)}{u_2 - u_1}} \ldots\ldots\ldots\ldots\ldots\ldots\ldots\ldots\ldots\ldots \quad (9)$$

h is the turbine's hub height, z_0 is a measure of the degree of roughness, and u is the velocity of air at h.

The variation in wake velocity relative to v_1 was determined from equations (8) and (9) by computing z_0 using wind values (h is 20 m, v is 3.79 m/s and data from the Metrological Service of Trinidad and Tobago [14] (h is 10 m, v is 3.2 m/s).

Resulting to: k_w = - 0.133, z_0 = 859.11.

As a result, it was possible to calculate the velocity entering rotor 2 as a function of both the rotor separation distance and the incoming wind speed as follows:

$$v_{\text{sec}\_rotor} = 0.6192v_1 \left(1 - \frac{0.3744}{1-0.266x}\right) \ldots\ldots\ldots\ldots \qquad (10)$$

The power coefficient (Cp) for the second rotor was calculated using previous procedure, but with a flow angle of -1 degree and new C_L of 0.8498 and C_D of 0.002245. The results are displayed in Table 3.

Table 3: Predicted Secondary Rotor Power Coefficients

Tip Speed Ratio, λ	3	5	7	9	11	13
Power Coefficient Cp	0.2876	0.3124	0.3453	0.3893	0.4094	0.4165
$\frac{\delta C_p}{\delta \lambda}$	-	0.0124	0.0165	0.022	0.01005	0.00705

For the secondary rotor, a tip speed ratio of 9 was selected from Table 3. As a result, the power obtained by the total turbine in relation to the incoming wind velocity, v_1, is as follows:

$$P = P_{pri\_rotor} + P_{\text{sec}\_rotor} \ldots\ldots\ldots\ldots\ldots\ldots\ldots\ldots \qquad (11)$$

$$P = Cp_{pri}\frac{1}{2}\rho A v_1^3 + Cp_{sec}\frac{1}{2}\rho A * \left(0.6192v_1\left(1 - \frac{0.3744}{1-0.266x}\right)\right)^3 .. \qquad (12)$$

Different values for v_1 and x were used to indicate the output power. The potential power production is depicted in Table 4 as it varies with wind speed and rotor separation.

Table 4: Potential power generation in relation to wind speed and rotor separation

Rotor Separation (x), m	Wind Velocity after passing through the primary rotor (x), m/s			Wind Velocity incoming to the secondary rotor (x), m/s			Primary Rotor RPM			Secondary Rotor RPM		
	1st Speed	2nd Speed	3rd Speed	1st Speed	2nd Speed	3rd Speed	1st Speed	2nd Speed	3rd Speed	1st Speed	2nd Speed	3rd Speed
3.00	3.169	4.155	5.459	1.393	1.686	2.769	284.765	396.324	547.854	63.925	85.845	115.308
2.75	3.172	4.156	5.457	1.434	1.938	2.822	284.647	396.125	547.854	65.602	88.398	118.829
2.50	3.169	4.156	5.457	1.477	1.992	2.884	284.846	396.006	548.123	67.324	91.028	122.457
2.25	3.169	4.155	5.456	1.520	2.047	2.945	284.744	396.120	548.012	69.090	93.736	126.197
2.00	3.170	4.155	5.457	1.565	2.103	3.004	284.542	396.089	547.914	70.909	96.524	130.051
1.75	3.169	4.155	5.458	1.611	2.161	3.066	284.323	396.583	547.843	72.763	99.395	134.022
1.50	3.170	4.154	5.457	1.659	2.220	3.129	284.322	397.004	547.666	74.673	102.352	138.114
1.25	3.169	4.155	5.457	1.708	2.381	3.193	285.002	396.432	547.334	76.632	105.396	142.332
1.00	3.169	4.154	5.457	1.758	2.344	3.259	284.843	396.612	547.477	78.643	108.532	146.676
0.75	3.172	4.155	5.454	1.810	2.409	3.326	284.754	396.547	547.059	80.706	111.760	151.157
0.50	3.168	4.155	5.457	1.863	2.475	3.395	284.543	395.854	547.244	82.824	115.084	155.773
0.25	3.169	4.157	5.457	1.926	2.543	3.464	284.812	396.344	547.548	84.997	118.508	160.530

Fig. 2: Potential output of power in relation to rotor separation wind speed
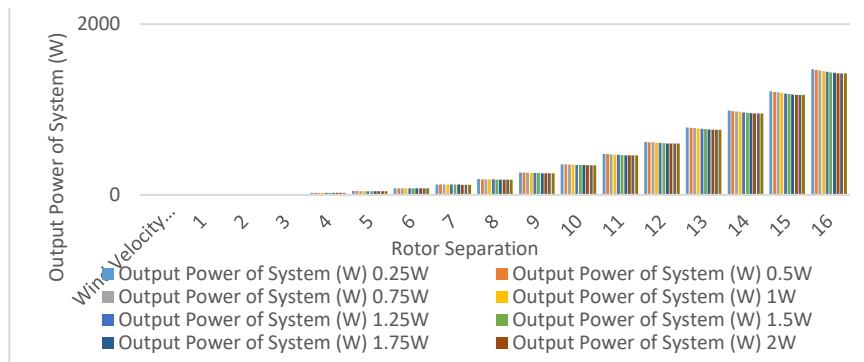
As illustrated in Fig. 2, the lowest rotor separation distance and fastest wind speed result in the highest output power. To provide an optimal power increase, the rotors should be as near to one another as is physically practicable.

The *Cp* for the complete system at 0.25 m rotor distance is:

$$C_p = \frac{Cp_{pri}\frac{1}{2}\rho A(v_1)^3 + Cp_{sec}\frac{1}{2}\rho A*\left(0.6192v_1\left(1-\frac{0.3744}{1-0.266x}\right)\right)^3}{\frac{1}{2}\rho Av_1^3} \quad \ldots\ldots \qquad (13)$$

Therefore, Cp is 58.69%.

It is possible to capture 58.69% of the kinetic energy of the wind, according to the blade element theory.

2.2. Stall Model Simulation

The 2 rotors were modelled with Qblade while taking into consideration root loss, tip loss, and 3 dimensional correction loss.

2.2.1. Primary Rotor

The tip speed ratio for the blade was established using the prior boundary conditions. The simulation's results were presented for angles of attack ranging from 10 degrees to 15 degrees with a variation of 0.5° using a maximum of 1000 iterations, *Rho* = 1.23, and a relaxation factor of 0.3 (Fig. 3).

Fig. 3. Correlation between the Primary Rotor's Tip Speed Ratio and the Power Coefficient
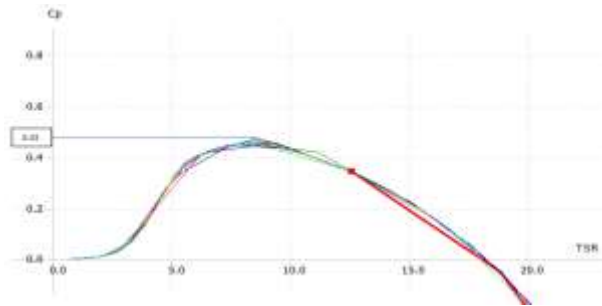
When the angle of attack is 6° and the tip speed ratio is 8.75 a *Cp* of 0.525414 was calculated from the simulation. The data were used to establish the optimal chord distribution for the blade, which is depicted in Table 5.

Table 5. Chord Distribution

Radial Position (m)	Chord length (m)
0	0.108013
0.05	0.0755337
0.1	0.057693
0.15	0.0465504
0.2	0.0389749
0.25	0.0335026
0.3	0.0293694
0.35	0.0261396
0.4	0.0235473
0.45	0.0214212
0.5	0.0196463

The main rotor turbine power (Fig. 4) was simulate using the wind field parameters of average wind speed 3.79 m/s, roughness length of 0.001 m, and 10% turbulence intensity.

Fig. 4: Power flow Simulation of the primary rotor

Equation (14) illustrates the wake velocity as a function of the rotor separation (*x*) based on the model:

$$v_{wake} = v_{in}\left(\frac{2.44272}{0.36x^2 - 0.1656x + 4.938}\right)\ldots\ldots\ldots\ldots\ldots\ldots \qquad (14)$$

An optimal wake velocity at 0.23 meters rotor distance was calculated using double differentiation.

2.2.2. Secondary Rotor

In order to accommodate a counter-rotation and have the same tip speed ratio of 8.75 as the main rotor, rotor 2 was modeled as a downwind turbine using the same wind field as the rotor 1 (Fig. 5).

Fig. 5: Power flow Simulation of the secondary rotor
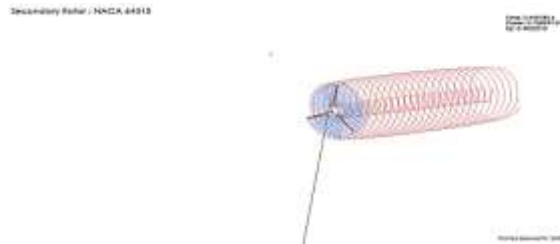
It was found that the secondary rotor's individual power coefficient was 0.4032213. Equation (15) was therefore used to calculate the total power output:

$$C_p = \frac{Cp_{pri}\frac{1}{2}\rho A(v_1)^3 + Cp_{sec}\frac{1}{2}\rho A * \left[v_1\left(\frac{2.14272}{0.36x^2 - 0.1656x + 4.938}\right)\right]^3}{\frac{1}{2}\rho A v_1{}^3}\ .. \qquad (15)$$

The system's power coefficient is thus 0.5599 at a rotor separation of 0.23 m.

Methodology

The system was built as illustrated in Fig. 6. It has two pillow block bearings with two coaxially mounted rotors on them. With the aid of nuts and bolts, the bearings are fastened to a piece of plywood. The plywood was supported by two stools. To ascertain the performance characteristics, speed and air flow sensors were added.

Fig. 6. The rotor setup

3.1. Arduino System

According to Fig. 7, the Arduino electrical system was created to capture both the rotor rotating speed and the intake flow wind speeds. A velocity sensor was built using an ultrasonic sensor from the kit that was placed at the entrance to the wind tunnel in addition to the RPM sensor. The ultrasonic sensor did not require any further signal processing, in contrast to the RPM sensor. A computer is used to power the Arduino system. The electronic system is made up of the following parts: Arduino Mega 2560 Controller (used to communicate computer-executable code to electrical components and receive signal from those components), 2 RPM sensors (used to record the rotor's rotational speed), 2 ultrasonic sensors (used to estimate the air velocity coming in), an LM 324 OP amp (used to condition the RPM sensor's signal), and a breadboard (used to establish power rails between electrical components). The code was written using C++ syntax in the free Arduino IDE.

Fig. 7. Arduino Electronic System
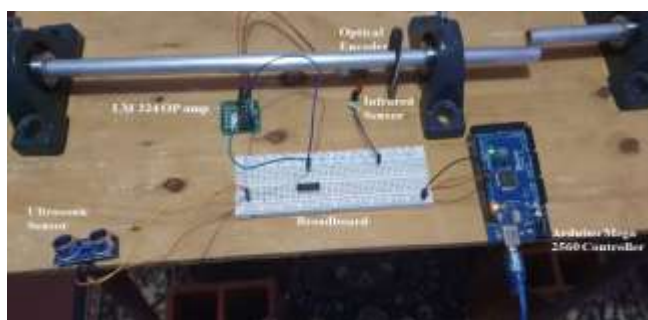
3.2. Air Study

Following an air analysis to adjust the turbine blades to the Trinidad environment, it was found that a NACA 64315 air foil would be the most suitable.

The apparatus was mounted on top of the roof of the mechanical engineering lab at the University of the West Indies (20 m high), using the Rainwise Portlog Weather Station. Over the course of two days, readings were taken every two minutes with the apparatus. The wind speed, wind direction, relative humidity, and other meteorological variables were recorded for 1440 readings. As illustrated by Fig. 8, the results for wind speed were plotted against time. A wind speed of 3.79 meters per second was observed in the figure. But a more cautious estimate for the wind speed was decided because of the significant standard deviation that takes place. A rated speed of 7 m/s was utilized for the design since 87.27% of the wind speeds observed are below that speed. The atmospheric characteristics calculator provided by the NACA was used to calculate a Reynold's Number of 478,650 and a Mach Number of 0.021 using this value.

**Fig. 8: Wind speeds results**
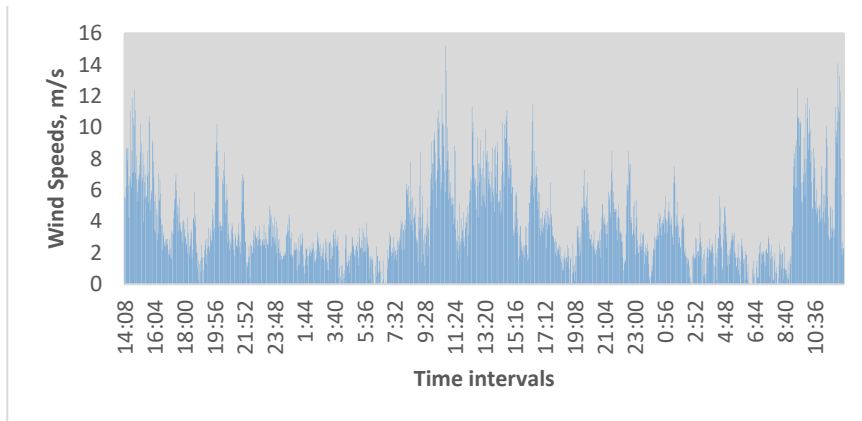
3.3 Selection of Airfoil

In line with NACA, deep camber airfoil having high aspect ratio should be selected at low wind speeds to avoid aerodynamic losses. For this study, five of the most popular airfoils with deep cambers and aspect ratios were chosen. These include the NACA 0012, Clark Y, Falcon II, NACA 64-315 and NACA 64-312. These airfoils were entered into XFOIL using a Reynold's number and Mach number computed from the research, and values for the lift to drag ratio (C_L/C_D) at various angles of attack were obtained. These results were presented on the Airfoil Comparison.

The NACA 64315 (Fig. 9) was chosen as the airfoil utilized to create the blade for this investigation, and its cross-section is depicted in Fig. 11. It was observed from Fig. 10 that the NACA 64315 had the maximum C_L/C_D at an angle of attack of 6°.
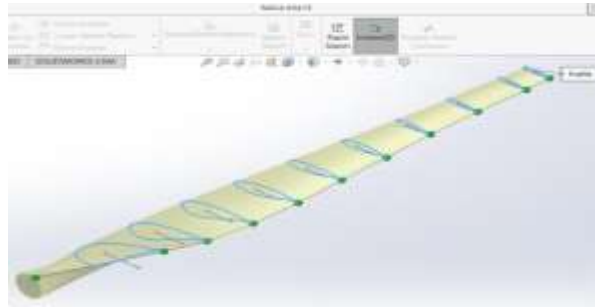
Fig. 9. NACA 64-315
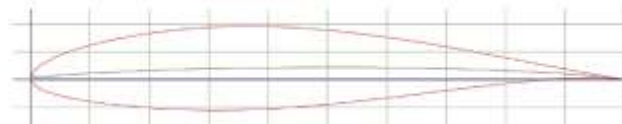
Fig. 10. Comparison of airfoils at varying angles of attack
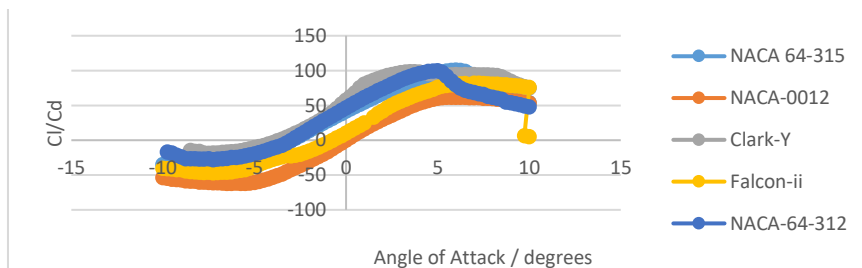
Fig. 11. Cross-section of the NACA 64–315 blade

3.4. Selection of Material

The materials used for the turbine should have some corrosion-resistant qualities because the air analysis revealed that throughout the testing time, the average relative humidity was 77%. It was decided to use a material with a high yield strength since the winds would cause the blades to bend. To reduce the amount of inertia it must overcome, the material should also have a low density. With comparison to other alloys, aluminum is less expensive and has these characteristics. However, due to the machine's constant use, the blades would be subject to significant cycle stress; as a result, a material with a high fatigue stress was chosen.

A fiberglass epoxy would be the best option for high fatigue strength, in addition to being an inexpensive material, as can be seen from the fatigue strength table. Cedar wood, which is cheap, light, and strong, was used to strengthen the fiberglass blades. A mixture of corrosion-resistant plastics was used to create the turbine's nacelle. As 6061 aluminum offers higher yield and fatigue strengths than other stainless steels while also being more readily available and less expensive, it was used to make the turbine shafts. The tower was constructed using common 11-gauge galvanized steel since it would be simple to obtain. In order to eliminate rocking movements and guarantee a strong footing for the turbine, the foundation was constructed of reinforced concrete. The interior parts were purchased from suppliers of standardized parts.

3.5. Data Collection and Testing

Following completion of the pilot scale, it was tested for a fixed tip speed ratio at various wind speeds and rotor separation distances.

The simulated and theoretical results that had been given previously in the research were validated by an experiment.

Required Apparatus

(i) Arduino Electronic System with RPM and Velocity Sensor Wind Tunnel in its completed state (ii) Computer to link the Arduino to and gather data from (iii) Wind Tunnel in its completed state (iv) 20-inch, 3-speed LASKO Fan.

Experimental Procedure

Experimental Setup (i) The fan was positioned 0.3 meters from the ultrasonic sensor (ii) The apparatus was configured with two rotors (iii)The fan was turned on at speed 1 while being watched for a steady velocity reading, which was then recorded. (iv) For speeds 2 and 3, the procedures were repeated (v)The rotors were mounted 3 meters apart on the shaft, and a grub screw was used to secure them. To secure them in position, the bearing was fastened to the plywood.

(vi) The fan was turned on at speed 1 and left running until both rotors reported a consistent rpm. Repeating step (vi) for speeds 2 and 3. Results were obtained after steps (v) through (vii) were performed for rotor separation lengths ranging from 2.75 to 0.25m at intervals of 0.25m.

3.5.1. Recorded Wind Velocity

The airflow ultrasonic sensor was used to measure the experimental wind speeds, and the Arduino's data on rpm was used to record the rpm values. The information obtained by the Arduino is displayed in Table 6. Results of the dynamic rotor test are displayed in Table 7.

Table 6. Lasko Fan Wind Speed

Speed Rating No.	Recorded Wind Velocity (m/s)
1	3.488
2	4.747
3	6.258

Table 7. Dynamic Rotor Test Experimental sResults

Rotor Separation (x), m	Wind Velocity after passing through the primary rotor (v), m/s			Wind Velocity incoming to the secondary rotor (v), m/s			Primary Rotor RPM			Secondary Rotor RPM		
	1st Speed	2nd Speed	3rd Speed	1st Speed	2nd Speed	3rd Speed	1st Speed	2nd Speed	3rd Speed	1st Speed	2nd Speed	3rd Speed
3.00	3.169	4.155	5.459	1.393	1.886	2.760	284.765	396.324	547.854	63.925	85.845	115.308
2.75	3.172	4.156	5.457	1.434	1.938	2.822	284.647	396.125	547.854	65.602	88.398	118.829
2.50	3.169	4.156	5.457	1.477	1.992	2.884	284.846	396.008	548.323	67.324	91.028	122.457
2.25	3.169	4.155	5.456	1.520	2.047	2.945	284.744	396.120	548.032	69.090	93.736	126.197
2.00	3.170	4.155	5.457	1.565	2.103	3.004	284.542	396.080	547.934	70.903	96.524	130.051
1.75	3.169	4.155	5.458	1.611	2.161	3.066	284.223	396.583	547.843	72.763	99.395	134.022
1.50	3.170	4.154	5.457	1.659	2.220	3.129	284.322	397.004	547.666	74.671	102.352	138.114
1.25	3.169	4.155	5.457	1.708	2.281	3.193	285.002	396.432	547.334	76.632	105.396	142.332
1.00	3.169	4.154	5.457	1.758	2.344	3.259	284.843	396.632	547.477	78.643	108.532	146.678
0.75	3.172	4.155	5.454	1.810	2.409	3.326	284.754	396.547	547.059	80.706	111.760	151.157
0.50	3.168	4.155	5.457	1.863	2.475	3.395	284.543	395.854	547.244	82.824	115.084	155.773
0.25	3.169	4.157	5.457	1.926	2.543	3.464	284.812	396.344	547.548	84.997	118.508	160.530

Results and Discussions

4.1 Comparative analysis of the Tip Speed Ratio with Fan Speed for the Primary Rotor

The comparative analysis of the tip speed ratio with the fan speed for the main rotor is shown in Fig. 12. Because the standard deviation for the several rotor separation tests is so negligible, the mean of the results may be calculated. Figure 12 showed a positive linear connection between the two variables, with the fan speed increasing as the tip speed ratio increases.
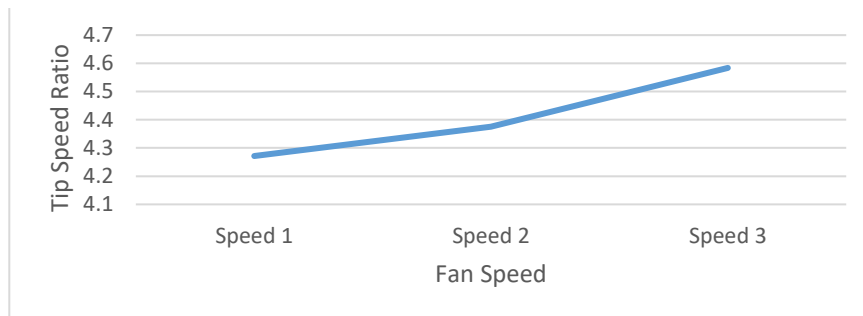
4.2 Comparative analysis of the Tip Speed Ratio with Fan Speed for the Secondary Rotor

The secondary rotor with rotor separations between 0.25 m and 3 m at intervals of 0.25 m is shown in Fig. 13 with the tip speed ratio compared to the fan speed. The tip speed ratio and fan speed are shown to have a positive linear relationship in each series. The biggest tip speed ratio is seen at the largest rotor separation distance (x is 3 m), while the smallest tip speed ratio is seen at the smallest rotor separation distance (x is 0.25 m) when the fan speed is 1 m/s.
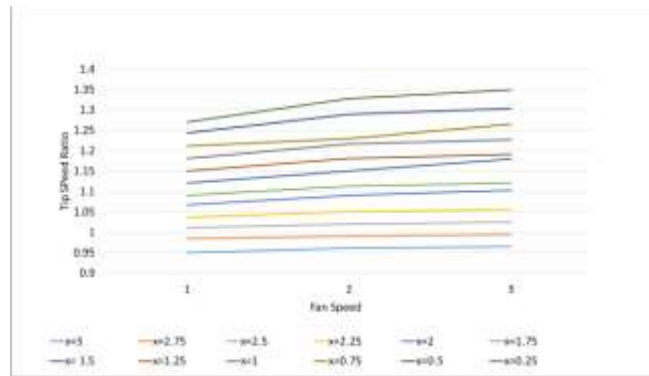
4.3 Comparative analysis of the Secondary Rotor's Tip Speed Ratio and Rotor Separation

The secondary rotor's tip speed ratio and rotor separation are contrasted in Fig. 14. The graph shows that the tip speed ratio and rotor separation are inversely related. The three series start (at x=3 m) but deviate from one another. It is a sign that the tip speed ratio likewise rises exponentially as speed rises.
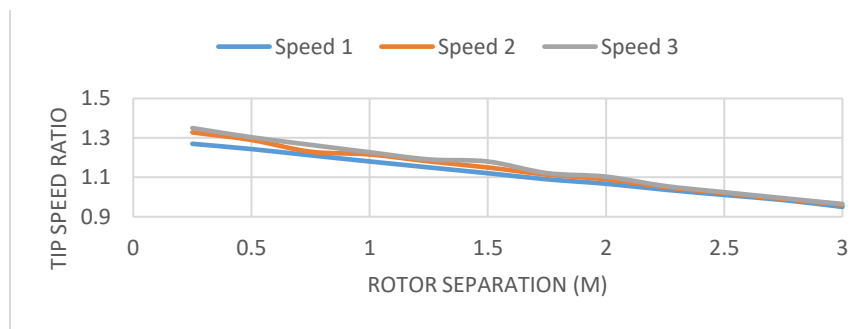
Fig. 12. Comparative analysis of the Tip Speed Ratio with Fan Speed (Primary Rotor)

Fig. 13. Comparative analysis of the Tip Speed Ratio with Fan Speed (Secondary Rotor)

Fig. 14. Comparative analysis of the Tip Speed Ratio with Rotor Separation (Secondary Rotor)

4.4 Comparative analysis of the total power with rotor separation

Figure 15 compares the total power with a rotor separation. It demonstrates the power gains for the three speeds, with speed 3 having the greatest power gains. Each line does, however, show a little positive gradient, showing that power improves as the space between the rotors gets smaller. Every series has a gradient that gets steeper as the pace goes up.

Fig. 15. Total power and rotor separation comparison
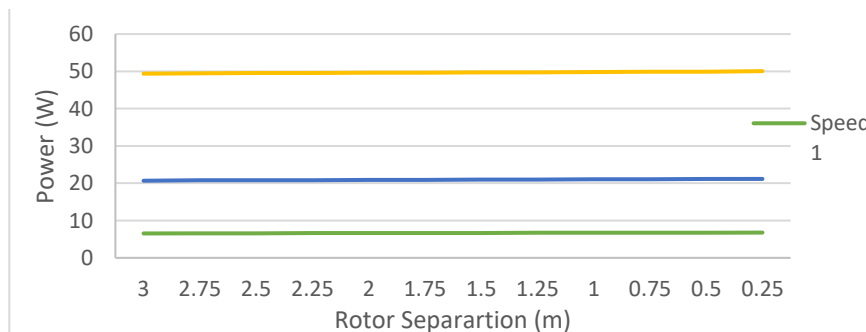
4.5. Comparative analysis of the power coefficient gains with rotor separation

The increase in power coefficient in response to changes in the spacing between the rotors is seen in Fig. 16. The rotor separation and power coefficient gain exhibit a negative linear relationship. The power coefficient increases more as the speed increases.

Fig. 16. Comparative analysis of rotor separation and power coefficient gain
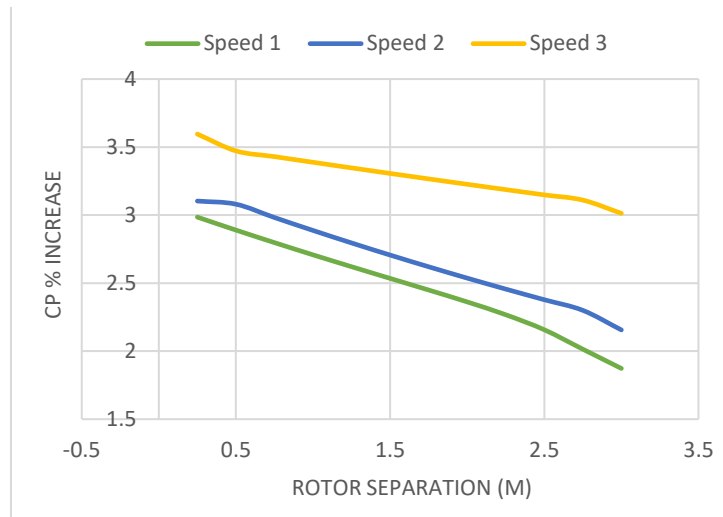
4.6. Comparative analysis of the power coefficient and rotor separation from simulation and experiment

The different power coefficients of the dual rotor system in response to rotor separation are shown in Fig. 17. The graph compares the power coefficient and rotor separation findings from the experimental data with the QBlade simulation. The power coefficient obtained from the simulation is greater than that obtained through experimentation. Similar R^2 results for each model indicate a good statistical correlation between simulation and experimental ways of measuring the power coefficient. R^2 values are a measure of the strength between dependent and independent variables.

As they pass the rotor in the stagnant air, the fast-moving air particles collide against the stationary air particles.

The air mass keeps travelling in the same direction as previously as a result of the impact. The air particles decelerate because of the loss of momentum caused by the impulse-momentum consistency. Since momentum and velocity are inversely correlated, the longer particles move, the more momentum they lose, reducing the wind speed over the travelled distance.

Additionally, the fast-moving particles deviate from their planned course as a result of these particles' three-dimensional collisions with stationary particles. The wind velocity decreases after passing through the rotor of

a wind turbine due to this effect, which also accounts for the turbulent wake velocity seen in the simulation.

In addition, compared to air particles, these particles disperse widely, over a significantly larger area. The flow continuity equation predicts that the velocity drops as the flow volume rises. This explains why the tip speed ratio drops down substantially from the main to the secondary rotor since the tip speed ratio depends on the velocity of the entering wind. Although the same wind stream that goes through the primary rotor also flows through the second rotor, the wind velocity is a little bit lower. It does not matter if there is usable kinetic energy in the air. It should be noted that greater speeds entering the primary side of the system result in higher wind velocities exiting and, consequently, higher secondary rotor tip speed ratios. With greater tip speed ratios and better power coefficients, the secondary wind turbine will operate as expected.

Regarding the correlation between power coefficient and rotor separation, it was found that the power coefficient increase as the two rotors became closer to one another. Both the experimental findings and the QBlade simulations support this behavior. The velocity drops as the distance between the two rotors gets less, according to the earlier-discussed concept. The results show that power should decrease as distance increases as power is directly related to velocity.

Since the generated wake velocity in the simulation was more than expected, the primary rotor's power coefficient should have been lower in the model. When compared to the outcomes anticipated by the simulation, the experimental findings were less favorable. The decrease is a result of manufacturing process faults. The blade was also built at a rated speed of 7 m/s, which the Lasko fan never achieves. The mechanical parts also had an additional safety factor built in and were sized for a maximum speed of 16 m/s. The system may have experienced extra rotor inertia as a result of this circumstance, which may have prevented the rotors from reaching the correct tip speed ratio.

The outcomes of this experiment support the Newman multi-actuator disk theory, which predicted that a dual rotor wind turbine will have a higher overall power coefficient [7]. This power coefficient improvement would not be practical, though, unless the financial advantages exceed the additional cost of creating and constructing the secondary turbine.

Fig. 17. Comparative analysis of the power coefficient and rotor separation for experiment and simulation
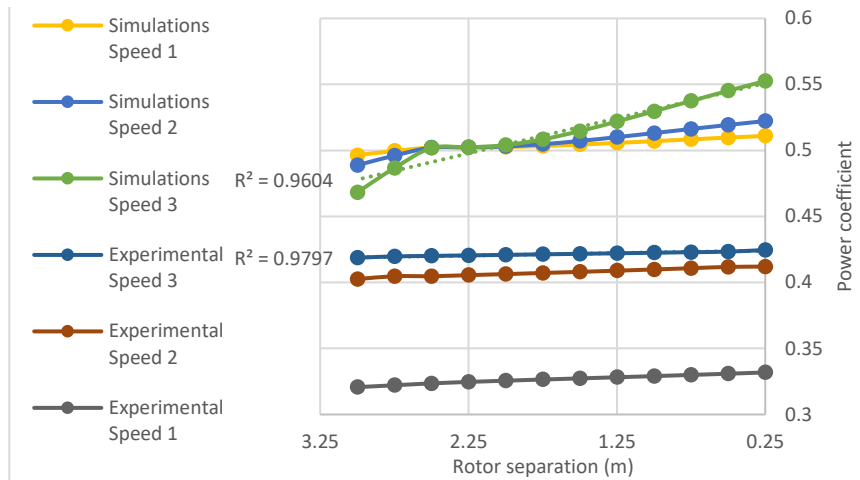
Conclusion

When rotor 2 is positioned behind rotor 1, it can take leverage of the disrupted airflow to extract up to 40 percent energy from allotted swept area than when using one rotor. A single-rotor propeller wastes energy by producing a lot of rotational or tangential air flow, which could be used instead.

This study used a constructed dual rotor horizontal axis wind turbine to conduct simulations and experimental analyses.

With the goal of maximizing lift force, the study investigates air flow analysis and design optimization of the air foil. The Reynold's number was calculated using the results of an accurate wind research, which also included the establishment of an accurate psychometric assessment of the air. The wind turbine was designed, adjusted, and made into a model in the form of a testing rig once the wind research was completed. The airfoil of the turbine that was most suited for the conditions was chosen. The testing was designed to verify the hypothesis examined, and the following results were obtained:

(i) The testing rig ran a little bit slower than the simulations.

(ii) Higher tip speed ratios were made possible by the rotors' larger incoming velocity.

(iii) The power gain increases as the rotor separation distance decreases.

(iv) At 0.25m rotor separation, a tip speed ratio of 4.584 for primary rotor and 1.35 for secondary rotor was recorded at an entering wind velocity of 6.258 m/s. These findings led to a system power coefficient of 42.46%, which translates into an additional 3.6% increase in power compared to a wind turbine with a single rotor.

Using RANS simulation, more research on the wake velocities should be done. According to the Jensen wake model [12], the area of overlap ratio influenced how strong the wake velocity was. In order to boost the efficiency of the entire system, additional research should be done by altering the size of the secondary rotor and employing a specialized secondary blade that will optimize the kinetic energy of the wind downwind.

Bibliography

1. IRENA. Renewable Energy Statistics (2020). International Renewable Energy Agency: Abu Dhabi, United Arab Emirates, 2020.
2. GWEC. Global Wind Report 2019; Global Wind Energy Council: Brussels, Belgium, 2020.
3. Offshore Wind Turbine SG 14-222 DD I Siemens Gamesa. Available online: https://www.siemensgamesa.com/en-int/productsand-services/offshore/wind-turbine-sg-14-222-dd (accessed on 13 July 2020).
4. Kumar P. S, Abraham A, Bensingh R. J. and Ilangovan S. (2013). "Journal of Scientific & Industrial Research 72".
5. Jung, S.N., No, T.-S., Ryu, K.-W., Aerodynamic performance prediction of a 30 kW counter-rotating wind turbine system, in Renewable Energy 30, pg. 631– 644, 2005.
6. Oprina G., Chihaia R.A., El-Leathey L.A., Nicolaie S., Băbuțanu C.A., Voina A. (2016) A Review On Counter-Rotating Wind Turbines Development. Journal of Sustainable Energy Vol.7, No.3, September, 2 ISSN2067-5534,2016.
7. Newman, B.G. (1986) Multiple Actuator-Disc Theory for Wind Turbines, in Journal of Wind Engineering and Industrial Aerodynamics, vol. 34, pg. 215-225, issue 3.
8. Chantharasenawong, C., Suwantragul, B., Ruangwiset, A. (2008) Axial Momentum Theory for Turbines with Co-Axial Counter Rotating Rotors, Commemorative International Conference of the Occasion of the 4th Cycle Anniversary of KMUTT Sustainable Development to Save the Earth: Technologies and Strategies Vision 2050: (SDSE2008) Bangkok, Thailand. 11-13 December 2008.
9. Appa, K. (2002) Energy Innovations Small Grant (EISG) Program (Counter Rotating Wind Turbine System), EISG Final Report, (California, US).
10. Rosenberg, A; Selvaraj, S; and Sharma, A. (2014). A Novel Dual-Rotor Turbine for Increased Wind Energy Capture. Journal of Physics: Conference Series, Volume 524, The Science of Making Torque from Wind 2014 (TORQUE 2014) 18–20 June 2014, Copenhagen, Denmark.
11. Milind Deotale, Abhishek Chavan, Abhishek Patil, (2018) Co-Axial Rotor Wind, Turbine Bhavesh Patil 1, IJARSE ISSN 23198354, vol 7 dated 7 April 2018.
12. Peña, Alfredo, Pierre-Elouan Réthoré, and M. Paul van der Laan. (2015) "On The Application of the Jensen Wake Model Using a Turbulence-Dependent Wake Decay Coefficient: The Sexbierum Case". Wind Energy 19 (4): 763-776. doi:10.1002/we.1863.
13. Wilson, R. E., P. B. S. Lissaman, M. James, and W. R. McKie. (1983) "Aerodynamic Loads on a Darrieus Rotor Blade". Journal of Fluids Engineering 105 (1): 53-58. doi:10.1115/1.3240940.
14. Trinidad and Tobago Metrological Service. https://www.metoffice.gov.tt/.